Electrochemical study on ion beam modified ternary composite of molybdenum disulfide, reduced graphene oxide and polypyrrole nanotubes

4.1 Introduction

In Chapter 2 and 3, the electrochemical properties of ternary nanocomposites prepared from MoS_2-rGO structures and conducting polymers (PEDOT and PPy) for supercapacitor applications were discussed. It is noticed that PPy based ternary system delivers high specific capacitance but the cycle life is found to be low. There are examples where electrochemical properties of supercapacitor electrodes can be improved by modifying the surface chemistry of the electrode by different surface modification techniques such as plasma irradiation, low energy ion irradiation and swift heavy ion irradiation [1-9]. Therefore, this chapter aims to improve the life span of the PPy based ternary system by modifying the surface of the electrode.

Among the various surface modification techniques, swift heavy ion (SHI) irradiation is a controlled surface tool that significantly tunes various properties of electrode material at electronic and molecular level [1]. As discussed in the 1st chapter, the parameters of SHI irradiation which take part in tuning the surface of an electrode are: (i) ion fluence, (ii) ion energy and (iii) ion species [2]. SHI irradiation modifies the surface of electrodes by transferring energy from the imparting ions to the target material in the form of energy loss $\frac{dE}{dx}$ (eV/Å), defines as energy deposition per unit length of the ion tracks. For SHI irradiation, inelastic collision is the dominant mechanism for energy transfer through ionization and excitation of the surrounding electrons. Conducting polymers are irradiation sensitive and many of the physio-chemical properties can be altered with this modification technique [3, 4]. MoS_2 and reduced graphene oxide (rGO) are also sensitive to SHI irradiation. Hannu-Pekka et al. [5] investigated the atomic structure of 2D MoS_2 sheet under electron irradiation. It was shown that prolonged electron irradiation on monolayer MoS_2 gives rise to agglomeration of sulphur vacancies. Similarly, SHI irradiation creates different types of defects in graphene such as adatom-vacancy pairs, stone-wales defects and di-vacancies [6]. The electrical properties of graphene can also be tuned by SHI

irradiation since mobility of the electrons and holes increase in the graphene sheets after SHI irradiation [7].

SHI irradiation is an efficient technique for modifying the conducting polymers in a controlled manner for supercapacitor application. The cycling stabilities of electrochemically deposited polypyrrole (66% to 94%) and polyaniline (81% to 94.6%) have been reported to be enhanced after 160 MeV Ni^{12+} SHI irradiation [3, 4]. SHI irradiation introduces cluster and columnar defect regions in the molecular structure of the conducting polymers and reduces the inter-chain electron hopping by cross-linking in the polymer chain giving rise to the increase in conductivity of the polymers [3]. The crystallinity of polypyrrole film increases upon 100 MeV SHI O^{7+} ion irradiation [8]. The SHI irradiation for supercapacitor application has been reported for bulk polymers [4] and for the binary nanocomposite of rGO and conducting polymer [9]. The 85 MeV C^{6+} SHI irradiated rGO and polypyrrole nanocomposite electrodes have shown enhanced capacitive behaviour with 346 Fg^{-1} of specific capacitance and cycling stability of 89% after 1000 cycles [9]. The comparative list of capacitive response and cycling stability of pristine and irradiated systems for supercapacitors is displayed in table 4.1.

Table 4.1: Comparison of specific capacitance and cycling stability of different electrode materials for supercapacitor:

Sl. No	Electrode material	Electrolyte	Modification technique	Specific capacitance	Cycling stability	Ref.
1	Few layer MoS_2	$TEABF_4$	None	14.75 Fg^{-1}	91% after 5000 cycles	[10]
2	MoS_2-Graphene	1M Na_2SO_4	None	11 $mFcm^{-2}$	39% after 1000 cycles	[11]
4	MoS_2-Polypyrrole	1M KCl	None	553.7 Fg^{-1}	90% of after 500 cycles	[12]
5	MoS_2/ Polyaniline	1M H_2SO_4	None	575 Fg^{-1}	98% after 500 cycles	[13]
6	MoS_2/PAni/ rGO aerogel	1M Na_2SO_4	None	618 Fg^{-1}	96% after 2000 cycles	[14]
7	MoS_2-rGO	1M KCl	None	1561 Fg^{-1}	72% after	[15]

	@Polypyrrole				10000 cycles	
8	Polyaniline	1M HCl	160 MeV Ni^{12+} SHI irradiation	243.4 Fg^{-1}	81% (pristine) 94.6% (irradiated) after 10k cycle	[3]
9	Polypyrrole	-	160 MeV Ni^{12+} SHI irradiation	205.5 Fg^{-1}	66% (pristine) 94% (irradiated) after 10k cycle	[4]
10	rGO/ Polypyrrole	1M KCl	85 MeV C^{6+} SHI irradiation	346 Fg^{-1} (irradiated) 299 Fg^{-1} (pristine)	77% (pristine) 89% (irradiated) after 1k cycles	[9]
11	MoS_2-rGO/PPyNTs	1M KCl	100 MeV O^{7+} SHI irradiation	1875 Fg^{-1}	91% after 10k GCD cycles	This work

Inspired from the above literature, this chapter discusses the SHI irradiation modifications on ternary MoS_2-rGO/PPyNTs nanocomposites. The ternary nanocomposite was irradiated with 100 MeV O^{7+} swift heavy ions at the fluence of $3.3x10^{11}$, $1x10^{12}$, $3.3x10^{12}$ and $1x10^{13}$ ions cm^{-2}. The structure, morphology and electrochemical performance of the pristine (unirradiated) and the irradiated nanocomposites have been evaluated and their potential application as electrode material for supercapacitor is discussed in this chapter. Facilities available at Inter University Accelerator Centre (IUAC), New Delhi were utilized for SHI irradiation.

4.2 Experimental:

4.2.1 Materials: Molybdenum disulphide (MoS_2) powder ($< 2\ \mu m$), graphite powder ($< 20\ \mu m$), Pyrrole monomer (98%) and Iron (III) Chloride ($FeCl_3$, 97% pure) were purchased from Sigma-Aldrich. Methyl orange indicator (SRL), cetyltrimethyl ammonium bromide (CTAB, Hi-media), laboratory reagents Sulfuric acid (H_2SO_4) (avantor), phosphoric acid (H_3PO_4) (avantor) and potassium permanganate (Merck

Emplura) were also used in different steps of the synthesis process. Nafion solution and Indium Tin Oxide (ITO) coated glass was purchased from Alfa Aesar and Macwin India, respectively.

4.2.2 Synthesis of MoS_2-rGO/PPyNTs composite: Ternary MoS_2-rGO/PPyNTs nanocomposites were synthesized as described in the section no. 3.2.3 of the Chapter no. 3.

4.2.3 Swift heavy ion irradiation on MoS_2-rGO/PPyNTs ternary nanocomposite: The ternary nanocomposite films were prepared by mixing active material with carbon black and nafion (binder) maintaining the mass ratio as 85:10:5 in DD water and ultrasonicated for 10 minutes. The obtained slurry was drop-cast in clean glass slide cut in 1x1 cm^2 dimensions for structural and morphological characterizations. For electrochemical characterization, films were casted on ITO coated glass, which was ultrasound cleaned with both DD water and acetone. The swift heavy ion (SHI) irradiation was performed on 1x1 cm^2 MoS_2-rGO/PPyNTs ternary nanocomposites films at Inter University Accelerator Centre (IUAC), New Delhi, India, at material science beam line under high vacuum of 10^{-6} Torr. The nanocomposites films were irradiated on both glass slides and ITO with 100 MeV O^{7+} swift heavy ions at four different fluences of $3.3x10^{11}$, 10^{12}, $3.3x10^{12}$ and 10^{13} ions cm^{-2}. Ion beam was projected to the films at an incident angle of 90°. The ion fluences were calculated with beam current and irradiation time according to the following equation:

$$Irradiation\ time(T) = \frac{\varphi \times A \times q \times e}{I} \quad [4.1]$$

where φ is the fluence, A is the area exposed to ion beam, q is the charge state, e is electronic charge and I is current. Area of irradiation was maintained to be 1x1 cm^2 for all samples, charge state is +7, e is $1.6x10^{-19}$ C and beam current was maintained to be 1 pnA (particle nanoampere) in our study. The ion doses for surface modification have been selected within the range of $3.3x10^{11}$-10^{13} ions cm^{-2}. The reason behind these fluences selection are: (i) no significant changes are expected in the structure and morphology for MoS_2 and rGO below $3.3x10^{11}$ ions cm^{-2}, and (ii) the conducting polymers burn beyond 10^{13} ions cm^{-2} irradiation fluence. The energy of the ions, electronic energy loss (S_e), nuclear energy loss (S_n) and the ion projected range in the MoS_2-rGO/PPyNTs electrodes were calculated in Stopping and Range of

ions in Matter (SRIM), software, 2008 and showed in table 4.2. The ion species is selected as 100 MeV O^{7+} because of its higher projected range (120.91 μm). Higher projectile range of the ion beam helps in uniform modification throughout the films with homogeneous electronic energy deposition which offers maximum utilization of bulk surface area of the electrode.

Table 4.2: Electronic energy loss (S_e), nuclear energy loss (S_n) and projected range for 100 MeV O^{7+} obtained from SRIM calculation for SHI irradiation of MoS_2-rGO/PPyNTs electrodes:

Ion Species	Ion energy (MeV)	Electronic energy loss S_e (eV/Å)	Nuclear energy loss S_n (eV/Å)	Projected Range (μm)
O^{7+}	100	54.33	0.029	120.91

4.2.4 Structural and morphological characterizations: Field emission scanning microscopy (FESEM) was performed with model JEOL JSM-7610F at 15 kV accelerating potential for morphological characterization of pristine and irradiated samples. X-ray diffraction (XRD) measurements were recorded for all the samples using a D8 X-ray diffractometer model Bruker AXS, Germany at a scan rate of 1 ^{o}/min. The Fourier transform infrared (FTIR) spectroscopy experiments were carried out using a Nicolet Impact 410 spectrometer for the pristine and irradiated samples in the form of KBr pellets in the range of 400-4000 cm^{-1}. Raman spectra were investigated with EZ Raman Enwave Optronics, USA spectrometer using a diode laser of excitation wavelength of 875 nm in the range of 200-3000 cm^{-1}. Contact angle measurements were carried out by using Data physics GmbH contact angle measurement system of model OCA 15 EC, Germany using sessile drop method with water and diiodomethane.

4.2.5 Electrochemical measurements: The electrochemical measurements were carried out in three electrode system (AUTOLAB 302N Modular Potentiostat Galvanostat, FRA32M Module/ Kanaalweg 29/G, 3526 KM Utrecht, Netherlands) at room temperature. 3 M KCl containing Ag/AgCl was used as reference electrode, platinum as counter electrode and active material loaded ITO was employed as

working electrode during all the electrochemical measurements. Nearly 1 mg of active material was cast on the ITO electrodes while preparing the working electrode. Electrochemical behaviour of the electrodes towards redox species were investigated using 10mM ferric-ferro solution in DD water containing 0.1 M KCl with cyclic voltammetry measurements within the potential window of -0.2 V to 0.8 V at scan rates in the range of 10 mVs^{-1} to 200 mVs^{-1}. Cyclic voltammetry (CV), Galvanostatic charge-discharge (GCD) and electrochemical impedance spectroscopy (EIS) were recorded to study the electrochemical performance using 1 M KCl solution as electrolyte for all the electrodes. CV measurements were carried out in a potential window of -0.3 V to 1.3 V within the capacitive potential range (CPR) at scan rates of 10, 20, 30, 40, 50, 70 and 90 mVs^{-1}. GCD measurements were evaluated with cut off potential from -0.3 V to 1.3 V at 1, 3, 5, 7, 9 and 11 Ag^{-1} of current densities. EIS data were recorded in 1 M KCl solution in AUTO FRA modular in a frequency range of 20 Hz-100 KHz.

4.3 Results and discussion

4.3.1 Field Emission Scanning Electron Microscopy: Figure 4.1 depicts the FESEM images of pristine and irradiated ternary MoS_2-rGO/PPyNTs nanocomposite films at different fluences of $3.3x10^{11}$, 10^{12}, $3.3x10^{12}$ and 10^{13} ions cm^{-2}. In the SEM image of pristine nanocomposites (Figure 4.1 a), the nanotubes have been observed and nanosheets are completely covered by the nanotubes. Upon increasing the electronic energy deposition, the surface of the electrodes is observed porous and the nanosheets can be seen along with the nanotubes from the irradiation fluence of $3.3x10^{12}$ ions cm^{-2}. The shapes of the nanotubes were not significantly affected by the bombardment of heavy ions at the low ion fluences. Fragmentations in the nanotubes were observed from the fluence of 10^{12} ions cm^{-2} (Figure 4.1 c). Interestingly, structural defect folding appears in the nanosheets at the irradiation fluence of $3.3x10^{12}$ ions cm^{-2} (Figure 4.1 f). Extended defects in the form of latent tracks in the nanosheets were noticeable from FESEM images (Figure 4.1 g). The nanotubes are completely damaged and some microscopic cracks could be seen in the nanosheets at the highest fluence used in this work. Thus, significant morphological changes are not observed at lower fluences ($<10^{12}$ ions cm^{-2}) but the nanotubes become unstable at the highest fluence of 10^{13} ions cm^{-2}. The nanotubes are damaged and mingled with the

nanosheets and cracks appeared in the nanosheets making the nanocomposite unstable at the fluence of 10^{13} ions cm^{-2}.

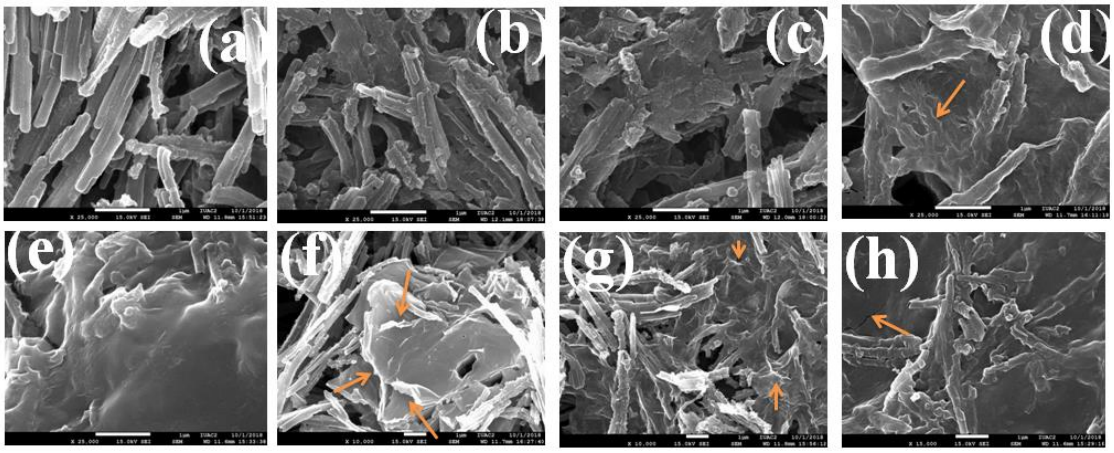

Figure 4.1: FESEM images of MoS_2-rGO/PPyNTs electrodes (a) pristine and irradiated with fluence of (b) $3.3x10^{11}$, (c) 10^{12} , (d) $3.3x10^{12}$, (e) 10^{13} ions cm^{-2} at magnification 25 kx and resolution 1 μm, (f) and (g) are at fluence $3.3x10^{12}$ ions cm^{-2} and (h) $1x10^{13}$ ions cm^{-2} at 1 μm resolution and different magnifications.

4.3.2 X-ray diffraction analysis: XRD spectra of bulk MoS_2, exfoliated MoS_2, rGO and PPyNTs are displayed in Figure 4.2 (i). Bulk MoS_2 possesses the major diffraction peaks at $2\theta = 14.42^o$, 35.84^o, 39.52^o, 44.16^o, 49.86^o corresponding to the planes of (002), (102), (103), (106) and (105) (JCPDS no. 77-1716). Exfoliated MoS_2 shows a small broad peak corresponding to (002) plane, suggesting successful exfoliation. Distinct peaks of rGO at $2\theta = 25^o and\ 42.97^o$ corresponding to (002) and (100) plane are observed after successful removal of oxygen containing groups by hydrothermal reduction of rGO at 200 ^oC without using any reducing agent. Pure polypyrrole nanotubes (PPyNTs) exhibit the characteristic broad amorphous humps at $2\theta = 25^o$ due to $\pi - \pi$ interaction of the polymer chains. The diffraction pattern of MoS_2-rGO/PPyNTs nanocomposite films were recorded before and after SHI irradiation and are displayed in Figure 4.2 (ii). Pristine MoS_2-rGO/PPyNTs film showed a broad hump around $2\theta = 15^o - 37^o$, which might be due to the overlapping of diffraction spectra of rGO nanosheets intercalated with MoS_2 ($2\theta = 19.71^o$) and amorphous PPyNTs ($2\theta = 25^o$). Small XRD peak at $2\theta = 14.42^o$ suggests the limited restacking of MoS_2 nanosheets in the pristine ternary film after drying the material. Upon SHI irradiation, the intensity of the diffraction peak at $2\theta =$

$15^o - 37^o$ increases (FWHM decreases) from the fluence of $3.3x10^{11}$ ions cm^{-2} to $3.3x10^{12}$ ions cm^{-2}, indicating the enhanced crystallinity of the nanocomposites.

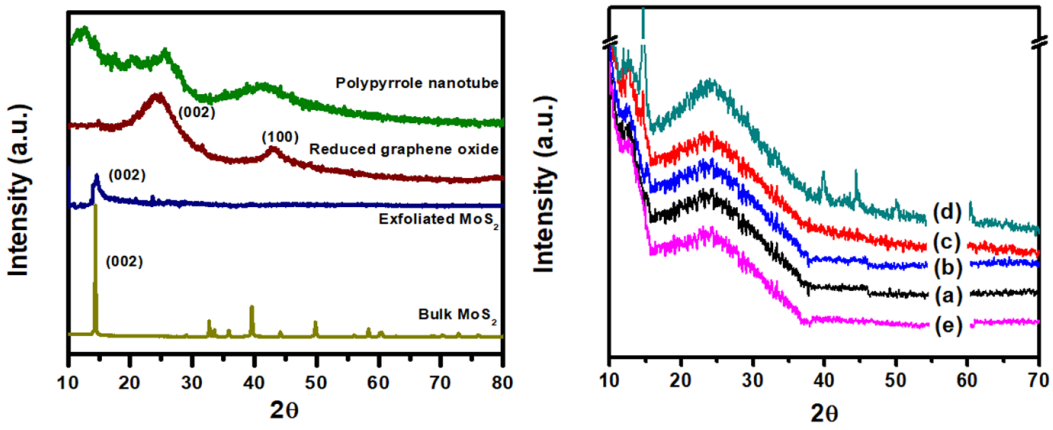

Figure 4.2: XRD pattern of (i) bulk MoS_2, exfoliated MoS_2, reduced graphene oxide and polypyrrole nanotubes and (ii) MoS_2-rGO/PPyNTs electrodes, (a) Pristine, and irradiated with fluence of (b) $3.3x10^{11}$, (c) 10^{12}, (d) $3.3x10^{12}$ and (e) 10^{13} ions cm^{-2}.

Table 4.3: Bragg angles and percentage of crystallinity determined from XRD patterns of pristine and irradiated MoS_2-rGO/PPyNTs electrodes at different fluence:

Sample Fluence / ions cm^{-2}	Bragg angle (2θ) / degree	Percentage of crystallinity (%)
Pristine	23.95	19.9
$3.3x10^{11}$	24.03	20.6
$1x10^{12}$	24.09	23.3
$3.3x10^{12}$	24.34	26.1
$1x10^{13}$	23.8	18.7

Percentage of crystallinity (X_c%) of the pristine and irradiated MoS_2-rGO/PPyNTs ternary nanocomposite films are calculated by comparing the area under the selected XRD peak to the total area according to equation no. 4.2 [16] and are given in Table 4.3 :

$$X_c = \frac{A_c}{A_c + A_a} \times 100\% \qquad [4.2]$$

where A_c is the area of the crystalline phase, A_a is the area of the amorphous phase and A_c+A_a is the total area under the XRD spectra. Crystallinity increases with the increasing ion dose up to the SHI fluence of $3.3x10^{12}$ ions cm^{-2} and decreases at the highest fluence of 10^{13} ions cm^{-2} employed in this work (table 4.3). Cross-linking /

recrystallization are the dominating processes over chain scission / bond breaking at high energy SHI irradiation (~100 MeV) of conducting polymers [17]. The polymer gets crystallized upon deposition of high energy due to stacking and ordering in the polypyrrole chains which may be attributed to cross-linking in the polymer chain or to the formation of single or multiple helices, resulting in the formation of crystalline regions in the irradiated films [18-20]. Hammering effects from swift heavy ions may cause the formation of periodic tracks and folding in the MoS_2 nanosheets [21]. These may be the cause of increased crystallinity in the MoS_2 nanosheets. At the highest fluence of 10^{13} ions cm^{-2}, the irradiated tracks overlap massively and each ion produces damages at the cylindrical disorder zone, which dominates the contribution from the primary amorphous zone and the electronic energy deposition is high enough to overcome the overall crystallinity of the nanocomposite, as a result the recrystalline MoS_2 peak disappears and overall crysallinity of the ternary nanocomposite decreases.

4.3.3 Fourier transforms infrared spectroscopy: FTIR spectroscopy has been performed to understand the modifications done by O^{7+} swift heavy ions on various functional groups present in MoS_2-rGO/PPyNTs nanocomposite films. FTIR spectra of pristine and MoS_2-rGO/PPyNTs nanocomposite irradiated with different fluences, are displayed in Figure 4.3 (a) in the range of 4000-450 cm^{-1}. The characteristic vibrational bands in ternary MoS_2-rGO/PPyNTs nanocomposites appear at 3428, 1565, 1308, 1231 and 1044 cm^{-1} corresponding to –OH vibrations, aromatic –C=C stretching vibrations, –CH bond vibration, C(O)–O stretching vibrations and sulfoxide group vibrations, respectively [22, 23]. FTIR peaks at 2940 cm^{-1} and 2927 cm^{-1} appear for the irradiated samples are corresponding to C-H bond vibrations, suggesting the cleavage of –C=H bonds, which decreases at the highest fluence. Intensity of the 1565 cm^{-1} band (–C=C) decreases with increasing fluence suggesting the successive bond breaking and degradation of the functional groups upon SHI irradiation [24]. The formation or degradation of in the functional groups after SHI irradiation can be understood with saturated track model according to the exponential relation given below [22]:

$$I(\emptyset) = I_0 \exp(-\sigma\emptyset) \qquad [4.3]$$

where σ is the degraded (or formation) cross sectional area of the selected functional group, $I(\emptyset)$ is the intensity of peak and I_0 is the normalized intensity of that peak in the pristine film. The slope of the plot of normalized peak intensity $\log\frac{[I(\emptyset)]}{I_0}$ vs. ion fluence gives the cross section σ. Figure 4.3 (b) shows the plot of logarithmic areal

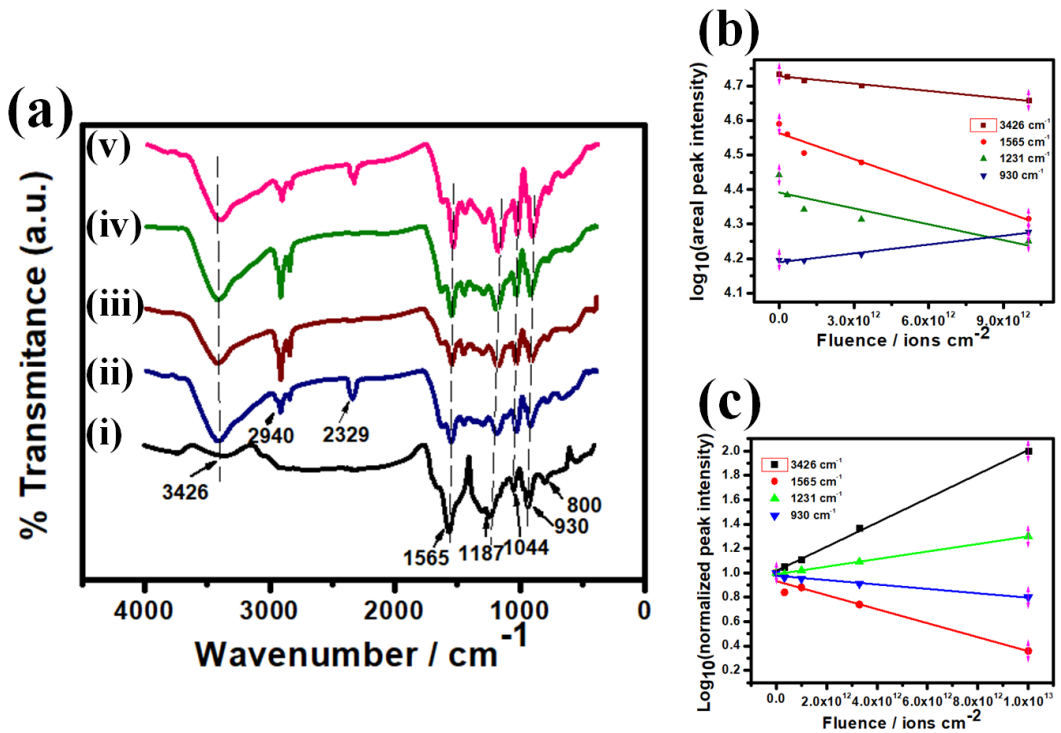

Figure 4.3: FTIR spectra of MoS_2-rGO/PPyNTs electrodes (a) pristine (i), and irradiated with fluence of (ii) $3.3x10^{11}$, (iii) 10^{12}, (iv) $3.3x10^{12}$, (v) 10^{13} ions cm^{-2}, (b) plots of areas of IR active modes of pristine and irradiated MoS_2-rGO/PPyNTs electrodes with fluences, (c) plots of $\log\frac{[I(\emptyset)]}{I_0}$ vs. fluences of the FTIR bands at 3426, 1556, 1231 and 930 cm^{-1} of MoS_2-rGO/PPyNTs electrodes.

peak intensity vs. ion fluence. As observed from Figure 4.3 (b) different IR sensitive bands have different sensitivity towards SHI irradiation as the slopes of areal peak intensity with ion fluence plot are different for different vibrational bands. Figure 4.3 (c) displays the $\log\frac{[I(\emptyset)]}{I_0}$ vs. fluence plots for –OH, –C=C, C(O)–O and Mo=O corresponding to 3426, 1556, 1231 and 930 cm^{-1} wavenumbers. The slopes from the linear fit of the plot of normalized peak intensity $\log\frac{[I(\emptyset)]}{I_0}$ vs. fluence have been calculated. The degraded (or formation) cross section are found to be $5.74x10^{-14}$ cm^2, $9.93x10^{-14}$ cm^2, $3.09x10^{-14}$ cm^2 and $1.8x10^{-14}$ cm^2 for the vibrational bands at 3426,

1556, 1231 and 930 cm^{-1}, respectively. The band corresponding to –C=C is highly sensitive for SHI irradiation with the highest formation or degraded cross section. The effective radius of formation or degraded of –C=C bond is 1.83 nm.

4.3.4 Raman spectroscopy analysis: Raman spectroscopy was performed to study the SHI irradiation effects on molecular vibrations in MoS_2-rGO/PPyNTs ternary nanocomposite. The Raman spectra of pristine and irradiated nanocomposites with O^{7+} SHI ions are displayed in Figure 4.4. Figure 4.4 (i) shows the Raman spectra of pristine (Figure 4.4 i a) and irradiated MoS_2-rGO/PPyNTs ternary nanocomposites with different fluences (Figure 4.4 i b-e). The characteristic E_{2g}^1 and A_{1g} modes of MoS_2 are observed around 400 cm^{-1}. The in-plane vibration of sulphur atoms towards

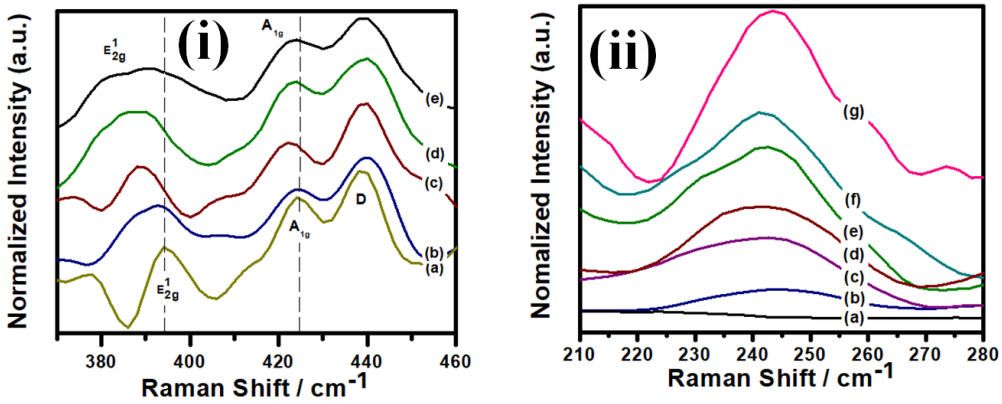

Figure 4.4: Raman spectra of MoS_2-rGO/PPyNTs ternary nanocomposites (i) pristine (a) and irradiated nanocomposite at fluences (b) $3.3x10^{11}$, (c) 10^{12}, (d) $3.3x10^{12}$, (e) 10^{13} ions cm^{-2}, and (ii) LA peak corresponding to (a) bulk MoS_2, (b) exfoliated MoS_2, (c) pristine MoS_2-rGO/PPyNTs, and irradiated at fluences (d) $3.3x10^{11}$, (e) 10^{12}, (f) $3.3x10^{12}$, (g) 10^{13} ions cm^{-2}.

Mo in the trilayer of MoS_2 gives E_{2g}^1 mode and the out-of-plane vibration of sulphur atoms, in the opposite direction gives A_{1g} mode in the Raman spectra of MoS_2 [25]. However, the LA peak around 235 cm^{-1} is the defect peak and appears due to the vibration of the longitudinal acoustic phonon near k point in brillouin zone of MoS_2 [26]. The appearance of sharp LA peak in Raman spectra suggests the increased concentration of defects with increasing SHI fluence [27]. For pure MoS_2, LA peak doesn't appear (Figure 4.4 ii a) due to the well arranged layered symmetric structure. Upon exfoliation with ultrasound, a small LA peak appears (Figure 4.4 ii b) as strain

arises in between the layers stacked. The pristine ternary nanocomposite is also enriched with a concentration of defects inherently present in it, as distinct LA peak appears in Raman spectra (Figure 4.4 ii c). The average inter-defect distance can be calculated using the formulae, $L_D = 1/\sqrt{\varphi}$, where φ is the ion density striking the surface of the nanocomposite film given by $\varphi = It/Ae$ here I is ion current, t is irradiation time, A is the exposed area and e is elementary charge [27]. The L_D value is calculated to be 17 nm at the fluence of $3.3x10^{11}$ ions cm^{-1} and decreases to 3.1 nm at the highest fluence. The peak positions and the FWHM of the both E_{2g}^1 and A_{1g} bands are plotted and shown in Figure 4.5. Red shift is observed for both the peaks (E_{2g}^1 and A_{1g}) (Figure 4.5 a) and magnitude of which distinctly increases with increasing fluence. The red shift occurs as a result of bond stretching leading to the reduction of effective force and force constant between the atoms giving rise to reduction in frequency [28, 29]. This shift suggests the appearance of tensile strain between the atoms and increase in bond length with increasing fluence [29]. Broadening of the peaks (Figure 4.5 b) observed for both the modes with the increasing fluence indicated the appearance of lattice defects [30]. Tensile strain can be calculated from Raman Spectroscopy using Gruneisen parameter (γ), which is a material dependant physical quantity related to Raman shift [29, 31] and can be calculated as follows:

$$\epsilon = (\omega_0 - \omega)/2\gamma\omega_0 \qquad [4.4]$$

where, ω_0 is the initial wave number and ω is the shifted wave number. From literature survey, γ is considered as 0.21 for E_{2g}^1 mode and 0.42 for A_{1g} mode [32]. Variation of strain in MoS_2 with SHI fluence is plotted and depicted in Figure 4.5 c. It is observed that strain increases with increasing fluence and is partially relaxed at the highest fluence. TMDCs are enriched with various kinds of structural defects and could be classified depending on their dimensionality [32]. Monolayer MoS_2 inherently contain the structural defects including vacancies, anti-sites, grain boundaries and edges etc. Wu Zhou et al. [32] have reported six different types of intrinsic point defects in monolayer MoS_2. Komsa et al. [5] reported that line defects of sulphur are created from the agglomeration of single sulphur vacancies when exposed to electronic irradiation. L Madauß et al. [33] studied the SHI irradiation effects of MoS_2 and rGO on SiO_2 substrate with 91 MeV Xe ions and reported the formation of nano-incisions and folding in both the materials. The induced strain by

SHI irradiation in MoS_2 gets relaxed beyond $3.3x10^{12}$ ions cm^{-2} (Figure 4.5 c) due to multiple overlapping of ion tracks at such great energy deposition. The variation of

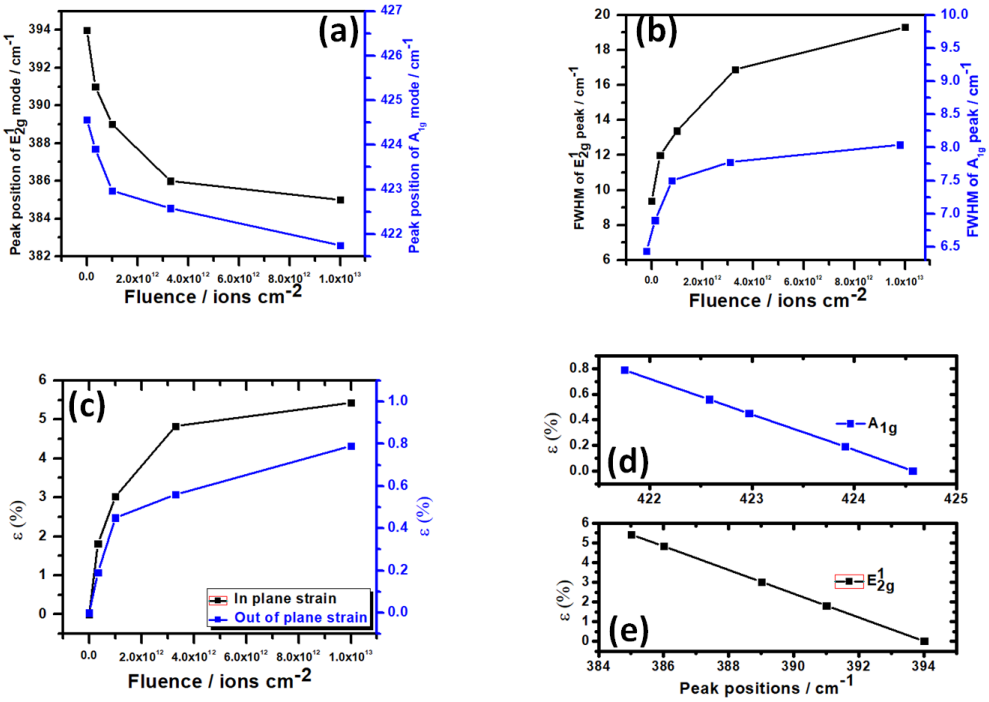

Figure 4.5: Analysis of Raman Spectra of MoS_2-rGO/PPyNTs electrodes (a) Raman shift in positions of E_{2g}^1 and A_{1g} modes of MoS_2 with fluence, (b) variation of FWHM of E_{2g}^1 and A_{1g} mode of MoS_2 vs. SHI irradiation fluence (c) Variation of strain of E_{2g}^1 and A_{1g} modes of MoS_2 vs. fluence, (d) In-plane and (e) out-of-plane strain as a function of peak position vs. fluence.

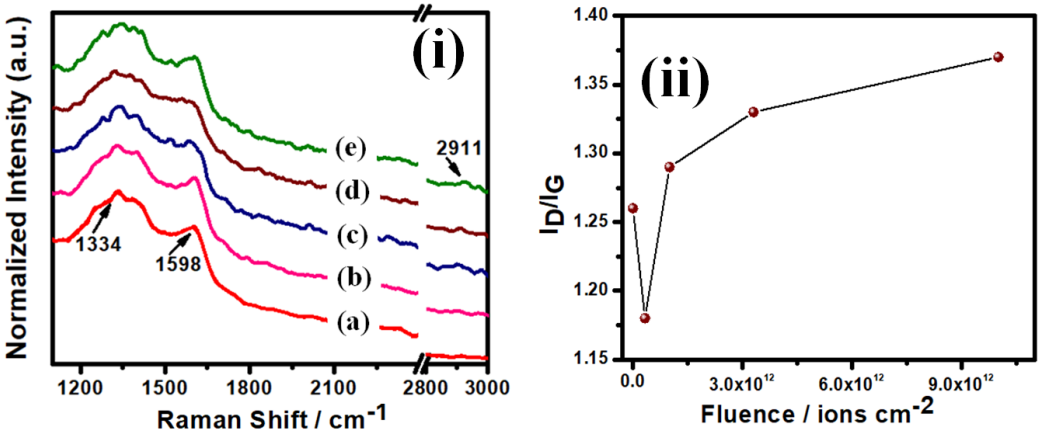

Figure 4.6: Raman spectra of (i) rGO in MoS_2-rGO/PPyNTs electrodes (a) pristine and irradiated nanocomposite at fluences (b) $3.3x10^{11}$, (c) 10^{12}, (d) $3.3x10^{12}$, (e) 10^{13} ions cm^{-2}, and (ii) plot of I_D/I_G ratio as a function of fluence.

strain with change in peak positions are depicted in figure 4.5 (d, e) for different SHI irradiation fluences for both the E_{2g}^1 and A_{1g} modes. The in-plane strain for E_{2g}^1 peaks and out-of-plane strain for A_{1g} peaks varies linearly with respect to peak positions. The linear dependency suggests that tensile strain changes along a- and c-axes [34].

The Raman spectra for the pristine and irradiated MoS_2-rGO/PPyNTs ternary nanocomposite shown in Figure 4.6 (i) also consist of characteristic Raman bands of rGO. In the nanocomposite, D and G bands are observed around 1331 cm^{-1} and 1605 cm^{-1}, respectively. The D band or defect band appears due to the A_{1g} symmetry phonons scattering at the defect sites and G peak corresponds to vibration of E_{2g} phonon in the sp^2 hybridized carbon atoms [35]. The relative intensity of the D band with the intensity of G band depends on the concentration of defects or disorder present in the graphene material. The ratio of relative intensity of D band (I_D) to the G band intensity (I_G) is called the disorder parameter (I_D/I_G). The disorder parameters are different for the pristine and irradiated samples and are plotted versus SHI irradiation fluence (Figure 4.6 ii). I_D/I_G ratio is smaller for the nanocomposite irradiated with the fluence $3.3x10^{11}$ ions cm^{-2} which may be due to annealing of rGO upon 100 MeV swift heavy ions irradiation [36]. The disorder parameter increases almost linearly from the fluence 10^{12} ions cm^{-2} to 10^{13} ions cm^{-2}, suggesting the increased concentration of defects and structural damages. In Raman spectra of rGO, D+D/ band (~ 2940 cm^{-1}) is also observed from fluence of 10^{12} ions cm^{-2} to 10^{13} ions cm^{-2} (Figure 4.6 i). D+D/ band arises from the combined vibration of phonons, around K and Γ, with different momenta. Presence of defect is required for activation of this mode [37]. The disorder parameter first decreases upto the fluence $3.3x10^{11}$ ions cm^{-2} and then starts increasing from the fluence of 10^{12} ionscm^{-2} to 10^{13} ionscm^{-2} (Figure 4.6 ii) where the D+D/ band appears simultaneously.

4.3.5 Contact angle analysis: Wettability of a supercapacitor electrode is an important parameter to understand the electrolyte permeability at the electrode surface and the electrode-electrolyte reactivity. The wettability studies were carried out with contact angle measurements, which were made for water (polar liquid) and diiodomethane (apolar liquid). The contact angle measurements for the pristine and irradiated MoS_2-rGO/PPyNTs ternary nanocomposite electrodes at different fluences are displayed in Figure 4.7 (a, b). The contact angle of the pristine nanocomposite

electrode is 86^o which increased to 97^o at fluence 10^{10} ions cm^{-2}. Contact angle decreased to 87^o and 79^o at fluence of $3.3x10^{11}$ and 10^{12} ions cm^{-2}, respectively which may be attributed to the breaking of polypyrrole nanotubes that makes the supercapacitor electrode more porous. As rGO is hydrophobic, the angle of contact increases to 85^o at the fluence of $3.3x10^{12}$ ions cm^{-2} and again decreases to 76^o at the irradiation dose of 10^{13} ions cm^{-2}, which may be ascribed to the formation of cracks in the nanosheets, as observed from FESEM.

The surface energies for pristine as well as unirradiated samples were calculated using Owens-Wendt-Rabel-Kaelble (OWRK) method [38] to study the polar and dispersive components according to the equation no (4.5):

$$\sqrt{\gamma_{sv}^{D}} + \sqrt{\gamma_{sv}^{P}}\frac{\sqrt{\gamma_{lv}^{P}}}{\sqrt{\gamma_{lv}^{P}}} = \frac{1}{2}\left[\gamma_{lv}\frac{1+cos\theta}{\sqrt{\gamma_{lv}^{D}}}\right] \tag{4.5}$$

where γ_{lv} is the surface free energy of the testing liquid (water or diiodomethane), θ is the contact angle. γ_{sv}^{D} and γ_{sv}^{P} are the dispersive and polar surface energy of the, respectively. The obtained values of total surface energy and its components are listed in Table 4.4: In 2D materials, atoms are covalently bonded and vdW force acts between two layers. From London dispersion theory, liquid can penetrate into the material either due to the interaction between permanent dipoles or through the formation of induced dipoles between two non polar components. Partial wetting transparency in graphene is observed due to surface defects or π- hydrogen bonding, although it consists of non-polar sp^2 hybridized carbon atoms [39]. Polar components arise from the interaction between permanent dipole moments. The random fluctuation of electron density in nearby area leads to the formation and interaction between induced dipoles which contributes to the dispersive components of surface energy [40]. The other vdW materials like MoS_2 and WS_2 are purely non-polar in nature. From the table 4.4, it is observed that the dispersive component is purely dominating the overall surface energy. The synthesized supercapacitor electrode consists of rGO, MoS_2 and PPyNTs, where rGO and MoS_2 are non-polar. The vdW individuals (rGO and MoS_2) offer long range london dispersive force and intrinsically contribute to the dispersive components in the surface energy. Moreover, SHI irradiation causes the random fluctuation of electron density from electronic energy loss. This may help in the formation of temporary dipoles in the electrode surface of

the irradiated electrodes in presence of electrolyte and as a result, the electrode/electrolyte interaction increases upon SHI irradiation.

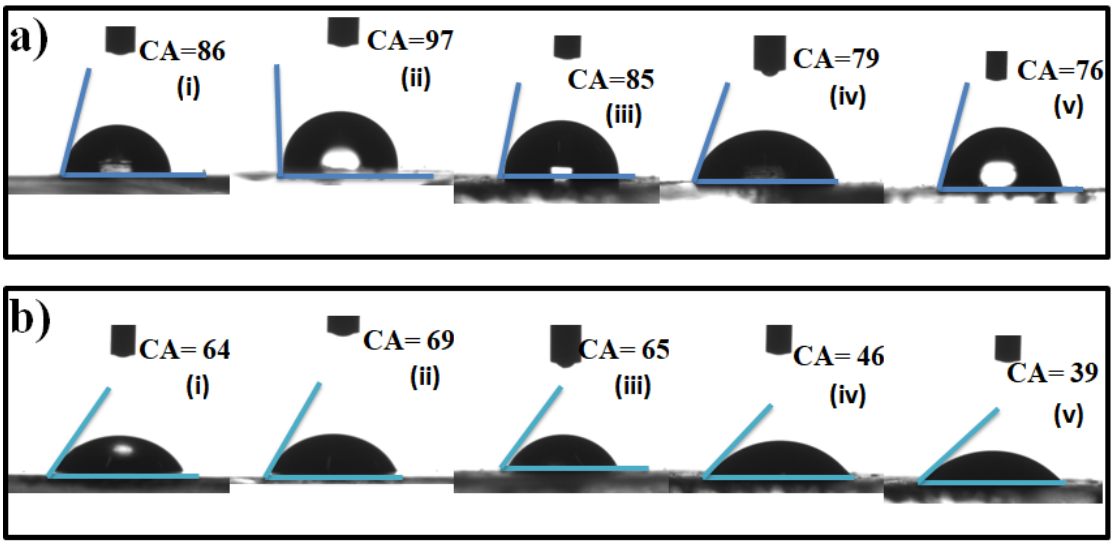

Figure 4.7: Contact angle measurements of MoS_2-rGO/PPyNTs electrodes (a) Contact angle with polar liquid water for (i) pristine, (ii) $3.3x10^{11}$, (iii) 10^{12}, (iv) $3.3x10^{12}$, (v) 10^{13} ions cm^{-2} SHI fluences and (b) with apolar liquid diiodomethane for (i) pristine and irradiation fluence at (ii) $3.3x10^{11}$, (iii) 10^{12}, (iv) $3.3x10^{12}$, (v) 10^{13} ions cm^{-2}.

Table 4.4: Contact angles of pristine and irradiated MoS_2-rGO/PPyNTs electrodes with water and diiodomethane and calculated values of polar, dispersive and total surface energies of the electrodes:

Irradiation Fluence/ ions cm^{-2}	Water Contact angle /degree	Diiodomethane Contact angle /degree	Surface energy dispersive γ_{sv}^{D} / mNm^{-1}	Surface energy polar γ_{sv}^{P} / mNm^{-1}	Surface energy Total γ_{sv} / mNm^{-1}
Pristine	86	67	26.28	3.42	29.7
$3.3x10^{11}$	97	69	23.43	1.08	24.51
$1x10^{12}$	79	65	25.7	6.46	32.15
$3.3x10^{12}$	85	46	36.47	1.7	38.17
$1x10^{13}$	76	39	40.1	3.45	43.64

4.3.6 Electrochemical behaviour of the electrodes towards redox species: The cyclic voltammograms (CV) of the pristine (Figure 4.8 a) and irradiated electrodes with fluence of $3.3x10^{11}$ ions cm^{-2} (Figure 4.8 b), 10^{12} ions cm^{-2} (Figure 4.8 c), $3.3x10^{12}$ ions cm^{-2} (Figure 4.8 d) and 10^{13} ions cm^{-2} (Figure 4.8 e) in 0.1 M KCl solution containing 10 mM $[Fe(CN)_6]^{-3/-4}$ at scan rates of 10, 30, 50, 70, 90, 100, 125, 150, 175 and 200 mVs^{-1} are displayed in Figure 4.8. A Pair of redox peaks is observed for all the electrodes due to the following redox reactions:

$$Fe^{2+} \rightarrow Fe^{3+} + e^{-} \qquad \text{(Oxidation)} \qquad [4.6]$$

$$Fe^{3+} + e^{-} \rightarrow Fe^{2+} \qquad \text{(Reduction)} \qquad [4.7]$$

The electro-catalytic behaviour was studied with the anodic peak current (Ipa) and cathodic peak current (Ipc) by calculating the separation between the anodic and cathodic peaks (ΔEp) in $[Fe(CN)_6]^{3-/4-}$. The bare ITO exhibits 1.15 mA anodic current and 0.92 mA cathodic current with peak separation of 230 mV, while pristine electrode exhibits 1.8 mA anodic current and 1.46 mA cathodic current with peak

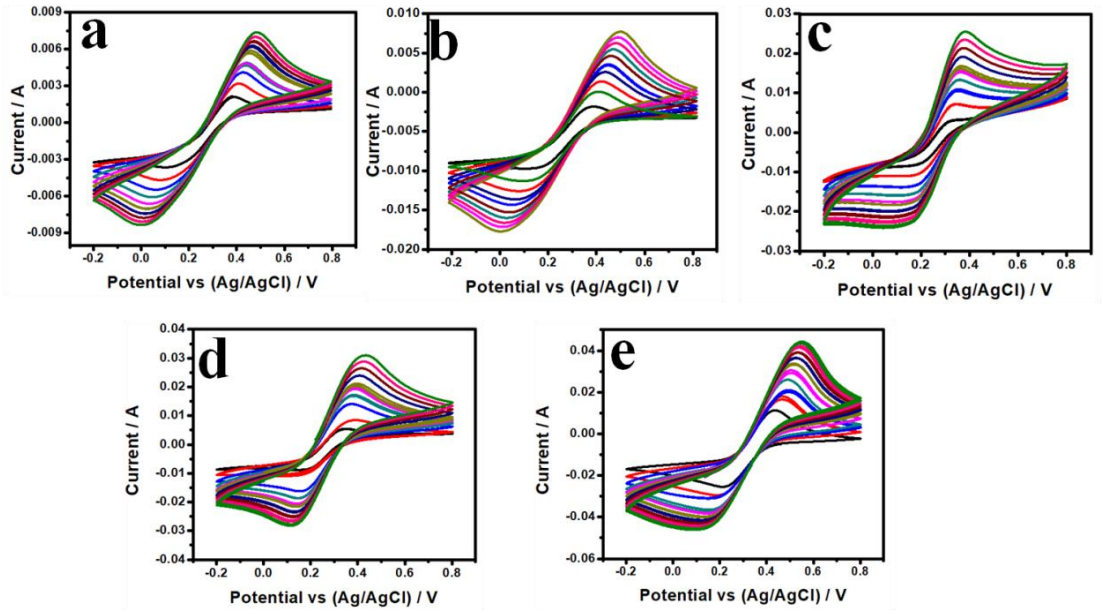

Figure 4.8: Cyclic voltammograms of MoS_2-rGO/PPyNTs electrodes (a) pristine and irradiated electrode with SHI fluence of (b) $3.3x10^{11}$, (c) 10^{12}, (d) $3.3x10^{12}$, (e) 10^{13} ions cm^{-2} in presence of 0.1 M KCl containing 10 mM $[Fe(CN)_6]^{-3/-4}$ at scan rates of 10, 30, 50, 70, 90, 100, 125, 150, 175 and 200 mVs^{-1}.

potential separation of 143 mV. These results indicate that charge transfer process is easier for the pristine electrode as compared to the bare ITO electrode. The ΔE_p value

decreases from 143 mV for the pristine electrode to 102 mV for the electrode irradiated at 3.3x10^{12} ions cm^{-2} for 10 mVs^{-1} scan rate. The decreasing value of ΔE_p suggests the increasing number of electrons participating in the charge transfer reaction as $\propto \frac{1}{\Delta E_P}$. The relative variation of anodic and cathodic peak currents with square root of scan rate $(\vartheta^{\frac{1}{2}})$ is depicted in Figure 4.9 a, b. The peak currents increase linearly with $\vartheta^{\frac{1}{2}}$ suggesting that the charge transport takes place in the electrode through diffusion controlled process and obey the Randles-Sevcik equation shown below:

$$I_p = 0.446\, nFAC \left(\frac{nF\vartheta D}{RT}\right)^{\frac{1}{2}} \quad [4.8]$$

where n is the number of electrons taking part in the redox reaction, F is faraday constant, A is area of the electrode, C is concentration of the redox species, ϑ is scan rate, R is gas constant, D is diffusion co-efficient and T is the temperature in K. The calculated values of cathodic slope, anodic slope and the electro-active surface area are displayed in table 4.5 for pristine and irradiated electrodes at different fluences. The table shows that the electro-active surface area continuously increases from the pristine to the highest fluence due to surface modification upon SHI irradiation. Figure 4.9 (c, d) shows the variation of cathodic and anodic peak potential vs. logarithmic of scan rate $\log\vartheta$ for all the electrodes. The charge transfer co-efficient ($\propto$) and the heterogeneous electron transfer rates (k_s) can be evaluated using laviron's theory [41] according to the following equations:

$$E_{pc} = E^0 - 2.3RT\frac{log\vartheta}{\propto nF} \quad [4.9]$$

$$E_{pa} = E^0 + 2.3RT\frac{log\vartheta}{(1-\propto)nF} \quad [4.10]$$

$$logk_s = \propto \log(1-\propto) + (1-\propto)log \propto - \log\frac{RT}{n\vartheta F} - \propto \frac{(1-\propto)nF\Delta E_p}{2.3RT} \quad [4.11]$$

where, E_{pc} is cathodic peak potentials and E_{pa} is anodic peak potentials, ΔE_p is peak to peak separation, n is electrons number, F is Faraday constant, R is gas constant and T is room temperature. The calculated values of $\propto$ and k_s are presented in the table 4.6, which shows that the values of transfer co-efficient and heterogeneous transfer rate increase up to the fluence of 3.3x10^{12} ions cm^{-2} and decrease at the highest fluence. The higher value of $\propto$ and k_s at 3.3x10^{12} ions cm^{-2} fluence signifies the faster transfer

of electrons from the electrolyte media to the electrode and improved charge transfer kinetics at the electrode-electrolyte interfaces.

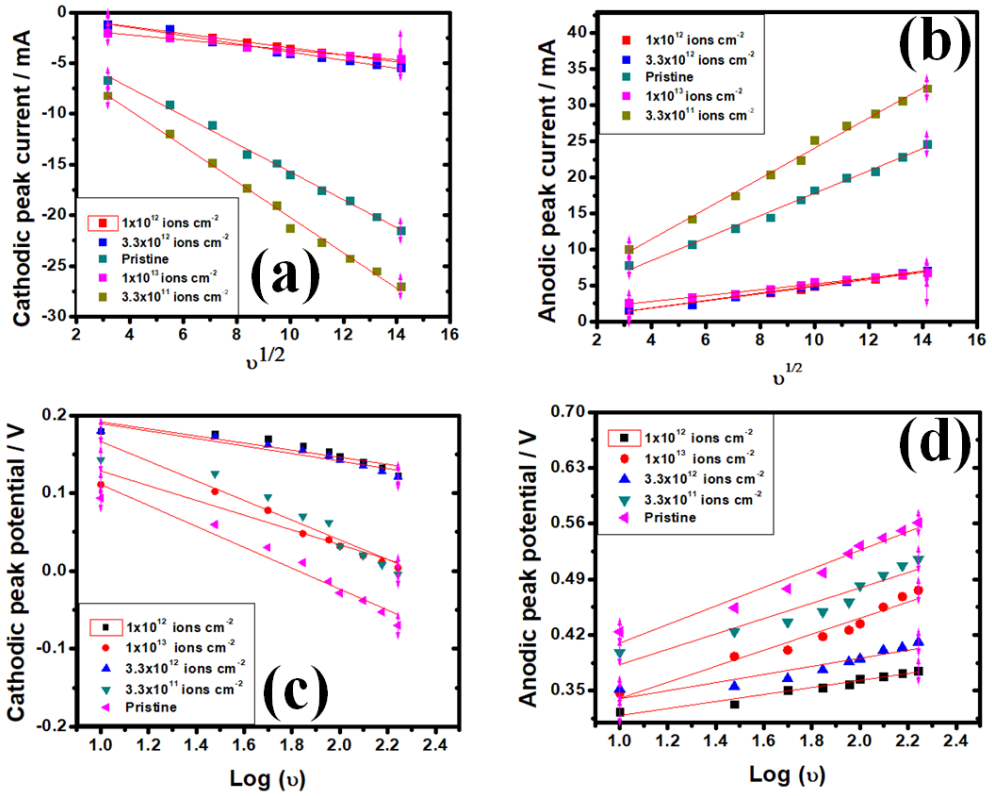

Figure 4.9: Analysis of cyclic voltammograms in 0.1 M KCl containing 10 mM $[Fe(CN)_6]^{-3/-4}$ solution. Variation of (a) cathodic and (b) anodic peak currents with square root of scan rate, $\vartheta^{\frac{1}{2}}$ and, (c) cathodic and (d) anodic peak potential vs. logarithmic of scan rate, $\log \vartheta$ for pristine and irradiated electrodes.

Table 4.5: Cathodic and anodic slopes of peak currents with square root of scan rate ($\vartheta^{\frac{1}{2}}$) and calculated values of electro-active surface from Randles-Sevcik equation of pristine and irradiated MoS_2-rGO/PPyNTs electrodes with variation of fluencies:

Irradiation Fluence /ions cm^{-2}	Anodic Slope	Cathodic Slope	Electro-active surface area /cm^2
Pristine	0.406	0.246	1.46
$3.3x10^{11}$	0.49	0.34	1.92
$1x10^{12}$	0.512	0.404	2.1
$3.3x10^{12}$	1.55	1.379	6.8
$1x10^{13}$	2.1	1.7	7.47

Table 4.6: Average heterogeneous rate constant, K_s (s^{-1}) and electron transfer coefficient (α) calculated from Laviron's model:

Irradiation Fluence /ionscm^{-2}	Average heterogeneous rate Constant, K_s/ s^{-1}	Electron transfer Coefficient , α
Pristine	0.47	4.98x10^{-2}
3.3x10^{11}	0.48	5.5x10^{-2}
1x10^{12}	0.51	5.9x10^{-2}
3.3x10^{12}	0.64	7.9x10^{-2}
1x10^{13}	0.49	5.1x10^{-2}

4.3.7 Cyclic Voltammetry (CV): Cyclic voltammograms of pristine and irradiated ternary MoS_2-rGO/PPyNTs nanocomposites are depicted in Figure 4.10 (a-e) measured in 1 M KCl electrolyte at scan rates of 10, 20, 30, 40, 50, 70, 90 mVs^{-1} in CPR (-0.3 V - 1.3 V). CV curves of the pristine (Figure 4.10 a) electrodes are observed to possess quasi-rectangular contour at lower scan rates (>40 mVs^{-1}) and the curves become slightly deformed in shape at higher scan rates (<50 mVs^{-1}) [42]. The quasi-rectangular geometry indicates the contribution of both electric double layer (EDL) capacitance from rGO and MoS_2 originating from the accumulation of charges at the electrode electrolyte interfaces and pseudocapacitance originating from the PPyNTs [43]. The current vs. potential response in the CV curve improves for the MoS_2-rGO/PPyNTs electrode irradiated with a fluence of 3.3x10^{11} ions cm^{-2} (Figure 4.10 b). The enhanced response in the CV pattern indicates the improved capacitive response of the supercapacitor electrode. At the fluence of 10^{12} ions cm^{-2} (Figure 4.10 c), the area under the CV curve increases and the electrode possesses higher capacitive response as compared to that of the 3.3x10^{11} ions cm^{-2} irradiated electrode. Interestingly, highest capacitive response was observed for the MoS_2-rGO/PPyNTs electrode modified with 3.3x10^{12} ions cm^{-2} with the highest mathematical area under the CV pattern. From XRD results, it is observed that PPyNTs start crystallizing from the lower fluence of SHI irradiation. Enhanced crystallinity in the ternary nanocomposite upon SHI irradiation facilitates formation of connected charge transfer paths in the electrode as a result of which electrolyte ions can penetrate deeper inside the electrode giving rise to enhanced capacitive responds. Contact angle measurement

results also corroborate the fact that the electrode-electrolyte interaction increases upon SHI irradiation. All the ternary electrodes exhibit the quasi-rectangular CV patterns except at the highest fluence. The CV pattern becomes almost rectangular at the highest fluence of 10^{13} ions cm^{-2}. The current vs. potential response degrades (Figure 4.10 e) and the capacitive response decreases at due to the fragmentation of PPyNTs, resulting in degradation of the charge transfer paths at the highest fluence of 10^{13} ions cm^{-2}.

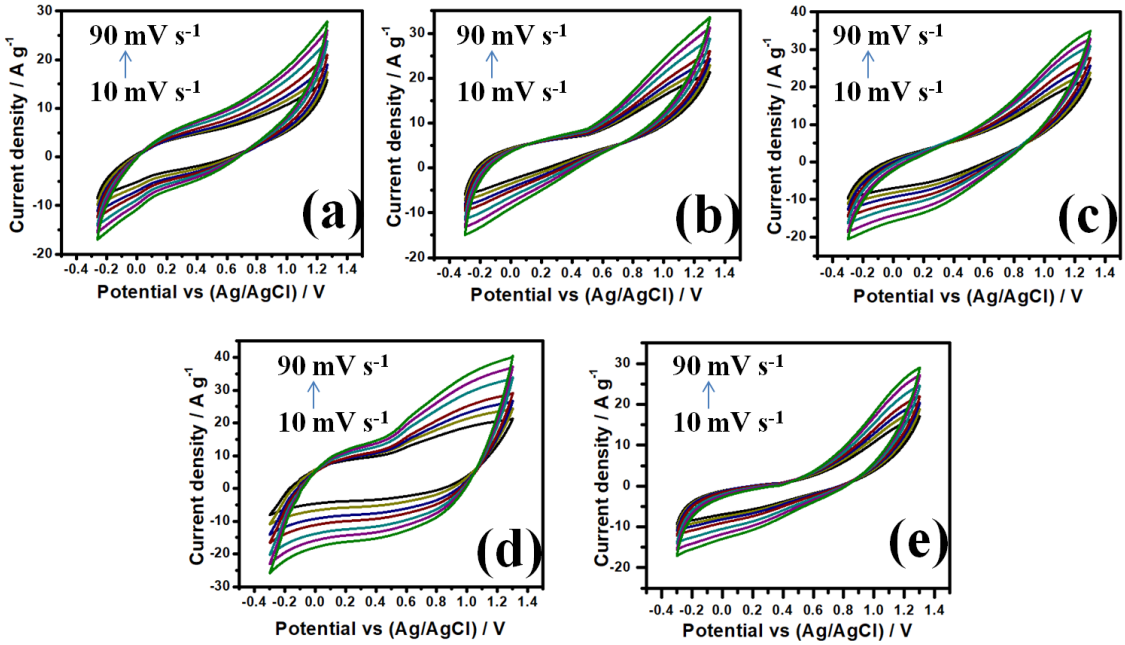

Figure 4.10: Cyclic voltammograms of (a) pristine and irradiated ternary MoS_2-rGO/PPyNTs nanocomposite electrodes with fluence of (b) $3.3x10^{11}$, (c) 10^{12} , (d) $3.3x10^{12}$ and (e) 10^{13} ions cm^{-2} in 1 M KCl electrolyte at scan rates of 10, 20, 30, 40, 50, 70 and 90 mVs^{-1}.

4.3.8 Galvanostatic charge-discharge: The GCD measurements of the pristine and irradiated electrodes have been conducted at a current density of 1 Ag^{-1} in 1 M KCl electrolyte in the potential range of -0.3 V to 1.3 V (verses Ag/AgCl) in order to study the capacitive response and other supercapacitor parameters. The GCD curves of the pristine and SHI irradiated MoS_2-rGO/PPyNTs electrodes at different fluence of $3.3x10^{11}$, 10^{12}, $3.3x10^{12}$ and 10^{13} ions cm^{-2} are shown in Figure 4.11 (i). Potential of the working electrode was recorded w.r.t. time against the reference electrode when a constant current was supplied to the counter electrode against the reference electrode.

The specific capacitance is calculated using the following equation,

$$C_{sp} = \frac{I \times \Delta T_d}{m \times \Delta V} \quad (4.12)$$

where $I, \Delta T_d, m, \Delta V$ are the constant discharge current applied, discharge duration of the electrode, mass loaded of the active material in the electrode and potential window in discharge process. The GCD curve of pristine MoS_2-rGO/PPyNTs electrode

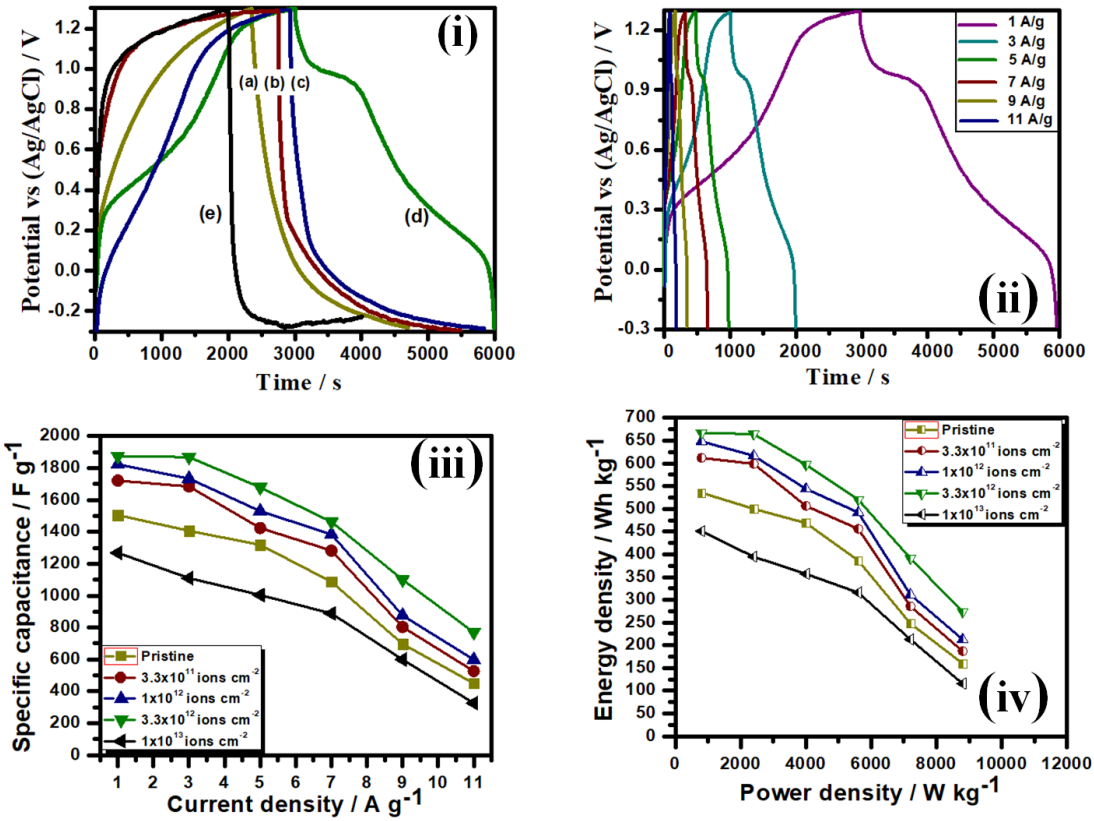

Figure 4.11: Galvanostatic charge-discharge (GCD) measurements of (i) ternary MoS_2-rGO/PPyNTs, (a) pristine and irradiated with fluences (b) $3.3x10^{11}$, (c) 10^{12}, (d) $3.3x10^{12}$, (e) 10^{13} ions cm^{-2} in 1 M KCl solution in 1 Ag^{-1} current density; (ii) GCD curves of $3.3x10^{12}$ ions cm^{-2} irradiated electrode at current densities of 1, 3, 5, 7, 9, 11 Ag^{-1} in 1 M KCl solution, (iii) rate capability of pristine and irradiated ternary MoS_2-rGO/PPyNTs electrodes and (iv) Ragone plot of pristine and irradiated ternary MoS_2-rGO/PPyNTs electrodes.

shows longer discharge duration and a high value of specific capacitance. The charging curve of the pristine electrode shows two slopes, the first slope is linear suggesting the EDLC contribution and the second part deviates from linearly due to pseudocapacitive contribution from the PPyNTs [15]. The irradiated electrodes are found to possess higher discharge period with enhanced specific capacitance for

supercapacitor energy storage. The GCD curve of the electrode irradiated with fluence of $3.3x10^{11}$ and 10^{12} ions cm^{-2} is observed to be more linear in both charging and discharging processes. This might be due to the fact that SHI irradiation widen up the pores of the electrode as observed from FESEM images. Moreover, PPyNTs become more aligned and crystalline. Highest gravimetric discharge duration is observed for the electrode irradiated with $3.3x10^{12}$ ions cm^{-2} with enhanced specific capacitance. At the highest fluence, the discharge duration and the capacitive responds degradeds, as the PPyNTs are completely damaged at such high electronic energy deposition. The microscopic cracks in the nanosheets also make the ternary nanocomposites unstable.

Kang et al. [44] reported the morphological effects on electrochemistry for SnO_2 electrodes of different morphology and obtained discharge capacity of 2137 $mAhg^{-1}$ for nanowires, 2304 $mAhg^{-1}$ for nanotubes and 1850 $mAhg^{-1}$ for nanopowder. The higher capacity obtained for the nanotubes was ascribed to higher electronic conduction and easy charge transfer with a higher aspect ratio which provided better electrolyte ion transfer and large number of reaction sites. Hussain et al. [3, 4] studied electrochemical performances of bulk $LiClO_4$ doped polypyrrole and HCl doped bulk polyaniline and obtained specific capacitance around 200 Fg^{-1} as well as enhanced cycling stability of the electrodes after SHI irradiation. Madhabi et al., [9] reported binary composite of rGO with polypyrrole nanotubes and obtained maximum specific capacitance of 288.57 Fg^{-1} with cycling stability of 77%, which increased to 346.28 Fg^{-1} and 89%, respectively, after 85 MeV C^{6+} SHI irradiation with optimum fluence of $2.2x10^{12}$ ions cm^{-2}. Here, MoS_2-rGO/PPyNTs electrode irradiated with fluence of $3.3x10^{12}$ ions cm^{-2} exhibits highest capacitive response of 1875 Fg^{-1} at current density of 1 Ag^{-1} with maximum enhancement of desired properties for electrochemical supercapacitors which is attributed to the improved crystallinity from XRD analysis, increased electrode-electrolyte interaction from contact angle measurements and enhanced electro-active surface area calculated from Randles Sevcik equation. The specific capacitance (C_{sp}) calculated from GCD measurements for pristine and irradiated MoS_2-rGO/PPyNTs electrodes are displayed in table 4.7.

The GCD measurements for the electrode irradiated with fluence of $3.3x10^{12}$ ions cm^{-2} are performed at 1, 3, 5, 7, 9 and 11 Ag^{-1} current densities and are displayed in Figure 4.11 (ii). The electrode exhibits specific capacitance of 1875 Fg^{-1}, 1868.5 Fg^{-1}, 1678.6 Fg^{-1}, 1462.5 Fg^{-1}, 1099.75 Fg^{-1} and 769.25 Fg^{-1} at 1, 3, 5, 7, 9 and 11

Ag^{-1} of current densities, respectively. The specific capacitance of the pristine and SHI irradiated MoS_2-rGO/PPyNTs electrodes for different SHI fluences are calculated at 1, 3, 5, 7, 9 and 11 Ag^{-1} current densities from GCD measurements and the rate capability of the electrodes vs. current density are shown in Figure 4.11 (iii). The pristine electrode possesses rate capability of 93.42% (3 Ag^{-1}), 87.57% (5 Ag^{-1}), 72% (7 Ag^{-1}), 46.3% (9 Ag^{-1}) of the initial specific capacitance, whereas the electrode irradiated with SHI fluence of $3.3x10^{12}$ ions cm^{-2} exhibits rate capability of 99.65% (3 Ag^{-1}), 90% (5 Ag^{-1}), 78% (7 Ag^{-1}), 58.6% (9 Ag^{-1}). The electrodes irradiated with fluence of $3.3x10^{11}$, 10^{12} and 10^{13} ions cm^{-2} show rate capability of 47%, 49% and 46%, respectively at 9 Ag^{-1} of current density. The increased electrode-electrolyte interaction from contact angle measurements, formation of charge transfer networks due to the increased crystallinity and the shorter diffusion paths after SHI irradiation may facilitate the enhanced rate capability in the irradiated electrodes. The calculated values of supercapacitor parameters Coulombic efficiency (η), energy density, power density and rate capability for 1 Ag^{-1} current density are displayed in the table. 4.7.

Table 4.7: Specific Capacitance (C_{sp}), Coulombic efficiency (η), Energy density (E), Power density (P) and Rate capability of the pristine and irradiated electrodes calculated from galvanostatic charge-discharge (GCD) measurements:

Irradiation Fluence / ions cm^{-2}	Specific Capacitance C_{sp} / Fg^{-1}	Coulombic efficiency η	Energy density E / $Whkg^{-1}$	Power density P / Wkg^{-1}	Rate capability at 7 Ag^{-1} current density
Pristine	1505	99.97%	535.15	800.05	72.2%
$3.3x10^{11}$	1721	99.98%	611.96	800.06	74.5%
$1x10^{12}$	1823	99.98%	648.23	800.06	75.9%
$3.3x10^{12}$	1875	99.98%	666.72	800.06	78%
$1x10^{13}$	1268	98%	450.88	800.06	70%

The Coulombic efficiency has been calculated from the following equation:

$$\eta = \frac{\Delta T_d}{\Delta T_c} \times 100 \quad (4.13)$$

where ΔT_d *and* ΔT_c stand for discharge and charging period, respectively. Almost 99.9% of Coulombic efficiency (table. 4.7) is observed for all the electrodes suggesting an efficient charge-discharge process with almost no loss of energy during

the electron transfer and a good reversibility of the electrode. Main challenge for a supercapacitor is to enhance the energy density vis-a-vis the conventional batteries. Hybrid supercapacitor electrodes with both the charge storage mechanisms possess higher energy density than that of the electrodes having single storage mechanism. The Ragone plot (power density vs. energy density) for pristine and SHI irradiated MoS_2-rGO/PPyNTs electrodes are depicted in Figure 4.11 (iv). The energy density and power density have been evaluated from GCD measurements at different current densities of 1, 3, 5, 7, 9 and 11 Ag^{-1} and analyzed using the equations (4.14) and (4.15):

$$\text{Energy density, } E = \frac{1}{2} C_{sp} (\Delta V)^2 \quad (4.14)$$

$$\text{Power density, } P = \frac{E \times 3600}{T_{dis}} \quad (4.15)$$

where, C_{sp}, ΔV and T_{dis} are the specific capacitance, potential window during discharge and discharge duration, respectively. The pristine MoS_2-rGO/PPyNTs electrode possesses power density of 800.05 Wkg^{-1} and energy density of 535.15 $Whkg^{-1}$ while the electrode modified with ion dose of $3.3x10^{12}$ ions cm^{-2} possesses impressive energy density of 666.72 $Whkg^{-1}$ maintaining almost the same power density at 1 Ag^{-1} current density. The electrodes irradiated with SHI fluence of $3.3x10^{11}$, 10^{12} and 10^{13} ions cm^{-2} exhibit energy density of 611.96 $Whkg^{-1}$, 648.23 $Whkg^{-1}$, 450.88 $Whkg^{-1}$, respectively and power density of 800.06 Wkg^{-1} for all the irradiated electrodes at 1 Ag^{-1} of current density. The ternary MoS_2-rGO/PPyNTs electrode irradiated with SHI fluence of $3.3x10^{12}$ ions cm^{-2} shows power density of 8800.78 Wkg^{-1} and energy density of 273.53 $Whkg^{-1}$ at 11 Ag^{-1} of current density, while the pristine electrode possesses power density of 8801.56 Wkg^{-1} with energy density of 159.87 $Whkg^{-1}$ at of current density of 11 Ag^{-1}. The pristine and irradiated electrodes maintain almost same power density at a specific current density, whereas energy density varies with change in current density. Highest energy density is obtained for the electrode modified with fluence of $3.3x10^{12}$ ions cm^{-2} and exhibited 41% of the initial energy density at 11 Ag^{-1} of current density as compared to the energy density of 29% of the pristine electrode. SHI irradiation facilities enhanced energy density by maintaining power density. The power density and the energy density at 1 Ag^{-1} of current density for the pristine and irradiated electrodes are displayed in table 4.7.

Internal resistance drop (IR drop) is the parameter controlling the efficiency of a supercapacitor electrode, higher value of which leads to the consumption of the electrolyte ions due to the development of over-potential at the electrode surface. With irradiation, it is observed that the IR drop continuously decreases up to a fluence of $3.3x10^{12}$ ions cm^{-2} and increases at the highest fluence as the charge transfer paths are degraded by swift heavy ions interactions with multiple overlapping of ion tracks. Cycling stability study is a crucial parameter for a supercapacitor electrode to understand its sustainability during practical application. The materials with EDLC mechanism possess extremely high cycle life during charge-discharge cycles with minimum degradation, whereas the pseudocapacitive materials scarify cycle life at the cost of high specific capacitance. Cycling stability was studied with galvanostatic charge-discharge cycles for the pristine and irradiated electrodes up to 5,000 cycles at 5 Ag^{-1} of current density and the specific capacitance with cycle numbers are

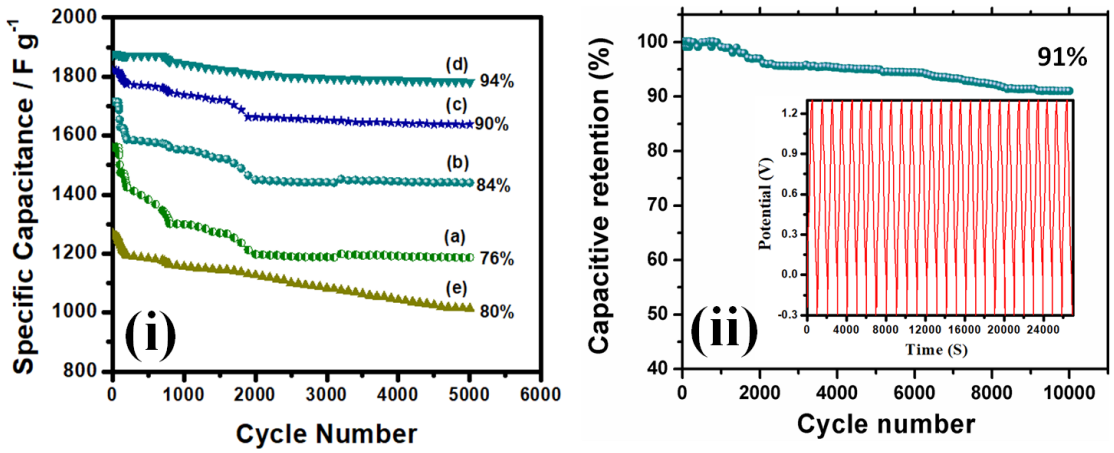

Figure 4.12: Cycling stability analysis MoS_2-rGO/PPyNTs electrodes. (i) Cycle number vs. specific capacitance of (a) pristine and irradiated with fluences (b) $3.3x10^{11}$, (c) 10^{12}, (d) $3.3x10^{12}$, (e) 10^{13} ions cm^{-2} in 1 M KCl solution in 5 Ag^{-1} current density up to 5000 cycles and (ii) cycle number vs. capacitive retention (%) for $3.3x10^{12}$ ions cm^{-2} irradiated electrode up to 10,000 cycles at current density of 5 Ag^{-1} in 1 M KCl electrolyte.

displayed in the Figure 4.12 (i). The specific capacitance of the pristine electrode showed 24% degradation after 5,000 GCD cycles. The irradiated electrodes with fluences of $3.3x10^{11}$, 10^{12}, $3.3x10^{12}$ and 10^{13} ionscm^{-2} possess cycling stability of 84%, 90%, 94% and 80%, respectively after 5,000 cycles. In our previous study [15], it was observed that MoS_2-rGO/PPyNTs nanocomposite showed 72% of cycling

stability after 10,000 cycles. The reason for lower cycling stability for the pristine electrode is: the pseudocapacitive material, PPyNTs undergoes volumetric swelling and shrinkage during GCD cycles which causes mechanical degradation in the electrode material. After irradiating the supercapacitor electrodes with swift heavy ions, the $\pi - \pi$ interaction in the PPyNTs chains increases due to enhanced crystallinity with increasing ion fluence. The oxidation states in PPyNTs were stabilized through $\pi - \pi$ interaction between the pyrrole groups giving rise to high cycling stability [45]. The cycling stability of the electrode irradiated with fluence of $3.3x10^{12}$ ions cm^{-2} has been studied up to 10,000 cycles at 5 Ag^{-1} current density (Figure 4.12 ii) and 91% of cycling stability is obtained. The nanocomposite irradiated at the fluence of $3.3x10^{12}$ ions cm^{-2} is more crystalline as compared to those irradiated at the other fluences and pristine as well. More crystalline nature provides increased $\pi - \pi$ interaction sites in the pyrrole chain and therefore the electrodes irradiated at this fluence become more stable as compared to the other electrodes.

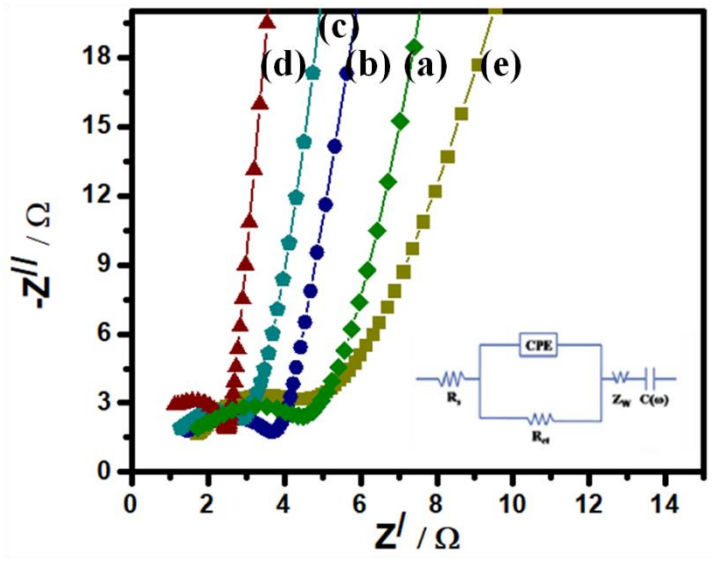

Figure 4.13: Nyquist plot of MoS_2-rGO/PPyNTs electrodes (a) pristine and irradiated with fluence (b) $3.3x10^{11}$, (c) 10^{12}, (d) $3.3x10^{12}$, (e) 10^{13} ions cm^{-2} in 1 M KCl electrolyte. Inset shows the equivalent circuit.

4.3.9 Electrochemical impedance spectroscopy analysis: The pristine and irradiated electrodes were characterized with electrochemical impedance spectroscopy to study the electrode kinetics during the electron transfer processes between the electrode and electrolyte in a frequency range of 10 μHz-10^5 Hz. To understand the interfacial properties of the electrodes variation of both the real and imaginary parts of complex

impedance are plotted as a function of frequency and depicted in Figure 4.13. The charge transfer processes at the electrode-electrolyte interface can be explained with randles equivalent circuit shown in the inset of Figure 4.13. Various elements of the equivalent circuit are: (i) R_s - equivalent series resistance, (ii) R_{ct} - charge transfer resistance, (iii) CPE - constant phase element and (iv) Z_w - Warburg impedance. The intercept of the semicircle in the high frequency region is R_s which gives the total intrinsic resistance of the electrode. Diameter of the semicircle is R_{ct}. CPE is the double layer capacitance (C_{dl}) in this case due to the presence of surface defects. If charge transfer is controlled by the diffusion process from the electrolyte to the electrode, warburg impedance appears towards the lower frequency region which is recognized by a linear spike inclined at an angle of 45^o. The calculated values of R_s and R_{ct} are presented in the table 4.8. It is observed from table 4.8 that R_s decreases for the irradiated electrode as compared to that of the pristine up to a fluence of $3.3x10^{12}$ ions cm^{-2}, which may be attributed to the enhanced crystallinity of the

Table 4.8: Equivalent series resistance (R_s) and Charge transfer resistance (R_{ct}) of pristine and irradiated electrodes determined from nyquist plots

Sample fluence (ions cm^{-2})	Equivalent series resistance (R_s) (Ω)	Charge transfer resistance (R_{ct}) (Ω)
Pristine	1.8	1.75
$3.3x10^{11}$	1.3	1.4
$1x10^{12}$	1.05	0.95
$3.3x10^{12}$	0.95	0.75
$1x10^{13}$	1.85	1.6

nanocomposite upon SHI irradiation. It may help in reducing the intrinsic resistance of the electrode as resistance of the electrochemical cell is constant. R_{ct} also decreases up to the fluence of $3.3x10^{12}$ ions cm^{-2}, since the charge transfer processes are efficient in the irradiated electrodes up to certain fluence as observed from the electro-catalytic behaviour of the electrodes. Moreover, irradiation produces disorder and interfaces in the electrode, which results in decrease in diffusion paths [9]. At the highest fluence of 10^{13} ions cm^{-2} both R_s and R_{ct} values were increased (table 4.8) because the electrode became unstable due to complete degradation of PPyNTs. The

vertical lines almost parallel to the imaginary axis are observed for all the electrodes towards the lower frequency region with slopes close to 1 indicating ideal capacitive behaviour.

4.4 Conclusions

The ternary nanocomposite films of MoS_2-rGO/PPyNTs were irradiated with 100 MeV O^{7+} Swift Heavy Ions (SHI) to tune the surface properties of the supercapacitor electrode. From morphological characterization (FESEM), it is observed that structural defects like folding and incision appear in the electrode at a fluence of $3.3x10^{12}$ ions cm^{-2}. XRD pattern reveals that the polymer's crystallinity increases up to a fluence of $3.3x10^{12}$ ions cm^{-2} due to cross-linking in the polymer chain and degrades at the highest fluence of 10^{13} ions cm^{-2}. MoS_2 in MoS_2-rGO/PPyNTs ternary nanocomposite also gets crystallized at the fluence of $3.3x10^{12}$ ions cm^{-2} due to the increased polymer crystallinity, hammering effects and formation of periodic tracks upon SHI irradiation. FTIR spectra suggest that different vibrational bands have different sensitivity towards SHI irradiation. The appearance of LA peak in the Raman spectra of exfoliated MoS_2 and MoS_2-rGO/PPyNTs ternary nanocomposite reveals the increasing concentration of defects density in MoS_2. In Raman spectrum of MoS_2-rGO/PPyNTs ternary nanocomposite, the disorder parameter corresponding to rGO first decreases and then continuously increases up to the highest fluence, indicating the increased defects or disorder in the nanocomposite. ($D+D^{/}$) band also appears in the RAMAN spectra of the nanocomposite due to the activation of various defect states after SHI irradiation. CV curves indicate that the capacitive response increases with increasing ion fluence up to the fluence of $3.3x10^{12}$ ions cm^{-2} and decreases at the highest fluence due to the degradation of PPyNTs. The discharge period in the galvanostatic curve is the highest for the fluence of $3.3x10^{12}$ ions cm^{-2} due to facile ion transport, enhanced electro-active surface area and improved electrode kinetics. The electrode irradiated at the fluence of $3.3x10^{12}$ ions cm^{-2} showed 91% of cycling stability after 10,000 galvanostatic cycles (5 Ag^{-1}) which as only 70% for the pristine electrode. 78% of rate capability at 7 Ag^{-1} of current density and 99.9% of Coulombic efficiency at the $3.3x10^{12}$ ions cm^{-2} fluence suggest a good rate capability and reversibility of the irradiated ternary electrode.

4.5 References

[1] Schmidt, B. Nanostructures by ion beams. *Radiation Effects and Defects in Solids*, 162: 171, 2007.

[2] Kamarou, A., Wesch, W., Wendler, E., Undisz, A., and Rettenmayr, M. Swift heavy ion irradiation of InP: Thermal spike modeling of track formation. *Physical Review B*, 73: 184107, 2006.

[3] Hussain, A.M.P., Kumar, A., Singh, F., and Avasthi, D. K. Effects of 160 MeV Ni^{12+} ion irradiation on HCl doped polyaniline electrode. *Journal of Physics D: Applied Physics*, 39: 750–755, 2006.

[4] Hussain, A.M.P., Saikia, D., Singh, F., Avasthi, D. K., and Kumar, A. Effects of 160 MeV Ni^{12+}ion irradiation on polypyrrole conducting polymer electrode materials for all polymer redox supercapacitor. *Nuclear Instruments and Methods in Physics Research B*, 240: 834-841, 2005.

[5] Komsa, H. P., Kurasch, S., Lehtinen, O., Kaiser, U., and Krasheninnikov, A. V. From point to extended defects in two-dimensional MoS_2: Evolution of atomic structure under electron irradiation. *Physical Review B*, 88: 3-15, 2013.

[6] Zenga, J., Yao, H. J., Zhang, S. X., Zhai, P. F., Duan, J. L., Sun, Y. M., Li, G. P., and Liu, J. Swift heavy ions induced irradiation effects in monolayer graphene and highly oriented pyrolytic graphite. *Nuclear Instruments and Methods in Physics Research B*, 330: 18-23, 2014.

[7] Kumar, S., Kumar, A., Tripathi, A., Tyagi, C., and Avasthi, D. K. Engineering of electronic properties of single layer graphene by swift heavy ion irradiation. *Journal of Applied Physics*, 123: 161533, 2018.

[8] Ramola, R.C., Chandra, S., Rana, J.M.S., Sonkawade, R.G., Kulriya, P.K., Singh, F., Avasthi, D.K., and Annapoorni, S. A comparative study of the effect of O^{+7} ion beam on polypyrrole and CR-39 (DOP) polymers. *Journal of Physics D: Applied Physics*, *41*(11): 115411, 2008.

[9] Devi, M., and Kumar, A. 85 MeV C^{6+} swift heavy ion irradiation of in-situ reduced grapheme oxide-polypyrrole nanotubes nanocomposite films for supercapacitor electrodes. *Electrochimica Acta*, 261:1-13, 2018.

[10] Pazhamalai, P., Krishnamoorthy, K., Manoharan, S., and Kim, S. J. High energy symmetric supercapacitor based on mechanically delaminated few-layered MoS_2

sheets in organic electrolyte. *Journal of Alloys and Compounds*, 771: 803-809, 2019.

[11] Bissett, M. A., Kinloch, I. A., and Dryfe, R. A. W. Characterization of MoS_2−Graphene Composites for High-Performance Coin Cell Supercapacitors. *ACS Applied Materials & Interfaces*, 7: 17388−17398, 2015.

[12] Ma, G., Peng, H., Mu, J., Huang, H., Zhou, X., and Lei, Z. In situ intercalative polymerization of pyrrole in graphene analogue of MoS_2 as advanced electrode material in supercapacitor. *Journal of Power Sources*, 229: 72-78, 2013.

[13] Huang, K.J., Wang, L., Liu, Y. J., Wang, H. B., Liu, Y. M., and Wang, L. L. Synthesis of polyaniline/2-dimensional graphene analog MoS_2 composites for high performance supercapacitor. *Electrochimica Acta*, 109: 587–594, 2013.

[14] Sha, C., Lu, B., Mao, H., Cheng, J., Pan, X., Lu, J., and Ye, Z. 3D ternary nanocomposites of molybdenum disulfide/polyaniline/ reduced graphene oxide aerogel for high performance supercapacitors. *Carbon*, 99: 26-34, 2016.

[15] Sarmah, D., and Kumar, A. Layer-by-layer self-assembly of ternary MoS_2-rGO@PPyNTs nanocomposites for high performance supercapacitor electrode. *Synthetic Metals*, 243: 75-89, 2018.

[16] Kumar, V., Sonkawade, R.G., Chakarvarti, S.K., Singh, P., and Dhaliwal, A.S. Carbon ion beam induced modifications of optical, structural and chemical properties in PADC and PET polymers. *Radiation Physics and Chemistry*, 81: 652–658, 2012.

[17] Banerjee, S., Deka, M., Kumar, A., and De, U. Ion Irradiation Effects in some Electro-active and Engineering Polymers: Studies by Conventional and Novel Techniques. *Defect and Diffusion Forum*, 341: 1-49, 2013.

[18] Nogami, Y., Pouget, J. P., and Ishiguro, T. Structure of highly conducting PF_6^--doped Polypyrrole. *Synthetic Meterial*, 62: 257-263, 1994.

[19] Qureshi, A., Singh, N.L., Shah, S., Kulriya, P., Singh, F., and Avasthi, D.K. Modification of polymer composite films using 120 MeV Ni^{10+} ions. *Nuclear Instruments and Methods in Physics Research Section B: Beam Interactions with Materials and Atoms*, 266(8):1775-1779, 2008.

[20] Sarmah, S., and Kumar, A. SHI irradiation effects on electrical and optical properties of PPy–SnO_2 nanocomposite. *Physica Status Solidi (A)*, 207(10): 2279-2287, 2010.

[21] Bolse, W. Self-organised nano-structuring of thin oxide-films under swift heavy ion bombardment. *Nuclear Instruments and Methods in Physics Research B*, 244: 8-14, 2006.

[22] Karimi, S., Feizy, J., Mehrjo, F., and Farrokhni, M. Detection and quantification of food colorant adulteration in saffron sample using chemometric analysis of FT-IR spectra. *RSC Advances*, 6: 23085-23093, 2016.

[23] Hazarika, J., and Kumar, A. 160 MeV Ni^{12+} ion irradiation effects on the structural, optical and electrical properties of spherical polypyrrole nanoparticles. *Nuclear Instruments and Methods in Physics Research B*, 318: 269-275, 2014.

[24] Nara, M., and Tanokura, M. Infrared spectroscopic study of the metal-coordination structures of calcium-binding proteins. *Biochemical and Biophysical Research Communications*, 369(1): 225-39, 2008.

[25] Li, H., Zhang, Q., Chong, C., Yap, R., Tay, B. K., Hang, T., Edwin, T., Olivier, A., and Baillargeat, D. From Bulk to Monolayer MoS_2: Evolution of Raman Scattering. *Advanced Functional Materials*, 22: 1385-1390, 2012.

[26] Guo, H., Sun, Y., Zhai, P., Zeng, J., Zhang, S., Hua, P., Yao, H., Duan, J., Hou, M., and Liu, J. Resonant Raman spectroscopy study of swift heavy ion irradiated MoS_2. *Nuclear Instruments and Methods in Physics Research B*, 381: 1-5, 2016.

[27] Mignuzzi, S., Pollard, A. J., Bonini, N., Brennan, B., Gilmore, I. S., Pimenta, M. A., Richards, D., and Roy, D. Effect of disorder on Raman scattering of single layer MoS_2. *Physical Review B*, 91: 195411, 2015.

[28] Ferralis, N., Maboudian, N., and Carraro, C. Evidence of structural strain in epitaxial graphene layers on 6H-SiC (0001). *Physical Review Letters*, 101: 156801, 2008.

[29] Shakya, J., Kumar, S., Kanjilal, D., and Mohanty, T. Work Function Modulation of Molybdenum Disulfide Nanosheets by Introducing Systematic Lattice Strain. *Scientific Reports*, 7: 9576, 2017.

[30] Kosacki, I., Suzuki, T., Anderson, H. U., and Colomban, P. Raman scattering and lattice defects in nanocrystalline CeO_2 thin films. *Solid State Ionics*, 149(1-2): 99-105, 2002.

[31] Li, X., Li, J., Wang, K., Wang, X., Wang, S., Chu, X., Xu, M., Fang, X., Wei, Z., Zhai, Y., and Zou, B. Pressure and temperature dependent Raman spectra of MoS_2 film. *Applied Physics Letters*, 109: 242101, 2016.

[32] Zhou, W., Zou, X., Najmaei, S., Liu, Z., Shi, Y., Kong, J., Lou, J., Ajayan, P. M., Yakobson, B. I., and Idrobo, J. C. Intrinsic structural defects in monolayer molybdenum disulfide. *Nano letters*, 13(6): 2615–2622, 2013.

[33] Madauß, L., Ochedowski, O., Lebius, H., Ban-d'Etat, B., Naylor, C.H., Johnson, A.C., Kotakoski, J. and Schleberger, M. Defect engineering of single-and few-layer MoS_2 by swift heavy ion irradiation. *2D Materials*, 4(1), 015034, 2016.

[34] Rice, C., Young, R. J., Zan, R., Bangert, U., Wolverson, D., Georgiou, T., Jalil, R., and Novoselov, K. S. Raman-scattering measurements and first-principles calculations of strain-induced phonon shift in monolayer MoS_2. *Physical Review B*, 87: 081307, 2013.

[35] Calizo, I., Balandin, A. A., Bao, W., Miao, F., and Lau, C.N. Temperature dependence of the Raman spectra of graphene and graphene multilayers. *Nano Letters*, 7: 2645-2649, 2007.

[36] Kumar, S., Tripathi, A., Singh, F., Khan, S.A., Baranwal, V., and Avasthi, D.K. Purification/annealing of graphene with 100-MeV Ag ion irradiation. *Nanoscale research letters*, 9(1):1-9, 2014.

[37] Cançado, L.G., Jorio, A., Ferreira, E.M., Stavale, F., Achete, C.A., Capaz, R.B., Moutinho, M.V.D.O., Lombardo, A., Kulmala, T.S., and Ferrari, A.C. Quantifying defects in graphene via Raman spectroscopy at different excitation energies. *Nano letters*, *11*(8): 3190-3196, 2011.

[38] Owens, D.K., and Wendt, R.C. Estimation of the surface free energy of polymers. *Journal of applied polymer science*, 13(8): 1741-1747, 1969.

[39] Kozbial, A., Li, Z., Sun, J., Gong, X., Zhou, F., Wang, Y., Xu, H., Liu, H., and Li, L. Understanding the intrinsic water wettability of graphite. *Carbon*, *74*: 218-225, 2014.

[40] Annamalai, M., Gopinadhan, K., Han, S.A., Saha, S., Park, H.J., Cho, E.B., Kumar, B., Patra, A., Kim, S.W., and Venkatesan, T. Surface energy and wettability of van der Waals structures. *Nanoscale*, 8(10): 5764-5770, 2016.

[41] Laviron, E. General expression of the linear potential sweep voltammogram in the case of diffusionless electrochemical systems. *Journal of Electroanalytical Chemistry and Interfacial Electrochemistry*, 01: 19-28, 1979.

[42] Lee, J.S.M., Briggs, M.E., Hu, C.C., and Cooper, A.I. Controlling electric double-layer capacitance and pseudocapacitance in heteroatom-doped carbons derived from hypercrosslinked microporous polymers. *Nano Energy*, 46: 277-289, 2018.

[43] Yoo, J.J., Balakrishnan, K., Huang, J., Meunier, V., Sumpter, B.G., Srivastava, A., Conway, M., Mohana Reddy, A.L., Yu, J., Vajtai, R., and Ajayan, P.M. Ultrathin planar graphene supercapacitors. *Nano letters*, 11(4): 1423-1427, 2011.

[44] Park, M.S., Kang, Y.M., Wang, G.X., Dou, S.X., and Liu, H.K. The effect of morphological modification on the electrochemical properties of SnO2 nanomaterials. *Advanced Functional Materials*, 18(3): 455-461, 2008.

[45] Kolek, M., Otteny, F., Schmidt, P., Mück-Lichtenfeld, C., Einholz, C., Becking, J., Schleicher, E., Winter, M., Bieker, P., and Esser, B. Ultra-high cycling stability of poly (vinylphenothiazine) as a battery cathode material resulting from π–π interactions. *Energy & environmental science*, 10(11): 2334-2341, 2017.